Ultraviolet–Visible-Near InfraRed spectroscopy for assessing metal powder cross-contamination: A multivariate approach for a quantitative analysis

Materials & Design 242 (2024) 113023

Contents lists available at ScienceDirect

Materials & Design

journal homepage: www.elsevier.com/locate/matdes

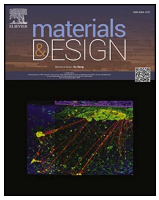

Ultraviolet–Visible-Near InfraRed spectroscopy for assessing metal powder cross-contamination: A multivariate approach for a quantitative analysis

Marta Ceroni [a,b], Federico Simone Gobber [a,b], Marco Actis Grande [a,b,*]

[a] Department of Applied Science and Technology (DISAT), Politecnico di Torino, Viale Teresa Michel 5, 15121 Alessandria, Italy
[b] National Interuniversity Consortium of Materials Science and Technology (INSTM), Via G. Giusti 9, 50121 Florence, Italy

ARTICLE INFO

Keywords:
Metal powder
Cross-contamination
Ultraviolet–visible-near infrared spectroscopy
Absorbance
Chemometrics

ABSTRACT

The last few years have seen an increasing use of spherical metals powders to produce bulk parts through metal forming technologies like Additive Manufacturing and Metal Injection Molding. This, coupled with the wide availability of metal powders, leads to a critical issue: contamination across different systems in different process steps. Consequently, it is necessary to find a new, fast, and reliable analysis sensible to tiny traces of contamination. This work evaluates the applicability of Ultraviolet–Visible-Near InfraRed (UV–Vis-NIR) spectroscopy, a technique providing information on powders' reflectance, for studying contaminated powders. This work focuses on assessing 3 binary systems obtained from the cross-contamination of 3 components (A92618, C10200 and S31603) in a low contamination range (from 0.5 vol% to vol. 6%) and in a high contamination range (25 vol% and vol.50%). After the UV–Vis-NIR analysis, multivariate analysis has been used to obtain quantitative results. Results show that, as the contamination level increases in the binary system, the shape of spectra changes and becomes progressively more similar to the contaminant one. The chemometric analysis allows the detection of the contaminant type and its concentration percentage in the contaminated powder.

1. Introduction

In recent years, the diffusion of metal-forming powders-based techniques has grown; this is mainly due to the increased use of Metal Injection Molding (MIM) [1] and Additive Manufacturing (AM) techniques like Electron Beam Melting, Direct Energy Deposition, Laser Powder Bed Fusion (L-PBF), and binder jetting [2,3]. MIM technology, as summarised by Basir et al. [4], is widely adopted due to many benefits it guarantees like low cost, material and design flexibility, good dimensional control and surface finishing, which result in near-net complex shape structures, excellent mechanical properties, little post-production scrap, and rapid prototyping. As reported by Narasimharaju et al. [5] and Abd-Elaziem et al. [6], additive manufacturing provides many advances, including significant time and cost savings, the possibility of obtaining complex shapes, high-density parts, and low material wastage. Among AM techniques, L-PBF is one of the more adopted; it consists of spreading layers of powder and melting selectively with a laser source, pass-by-pass, as explained by Chowdhury et al. [7]. Commercially, L-PBF devices are usually equipped with red laser sources characterised by wavelengths in the range of 1064–1080 nm as revealed by Jiang et al. [8], but they can also be equipped with blue or green laser sources, as highlighted by Asano et al. [9] and Siva Prasad et al. [10].

The increasing use of powder-based technologies is leading to the study and production of new metal powders of elemental metals and alloys (Soong et al. [2], Wang et al. [11]). New powder systems are being studied and atomised, particularly in the field of Al alloys (Monti et al. [12]), Cu-based materials (Shi et al. [13]) and Fe −based powders, as reported by Silva et al. [14] in terms of stainless steels or by Sarriegui et al. [15] as powders for magnetic application. Generally the same instrument is used for the evaluation of the powder properties or for the processing of different materials. Considering the growing number of powder systems, in case working and/or storage conditions are not adequately controlled, cross-contamination might occur. Cross-contamination can be more or less catastrophic depending on the mechanical/physical properties of the contaminating powder compared to the contaminated one and its percentage. Among the possible defects that may arise, the reduction of mechanical properties of the final products and the inconsistent layer adhesion due to the difference in melting temperature of powders must be mentioned as demonstrated by Brandão et al. [16] and Zhang et al. [17]. Cross-contamination can take place in several different process steps, like during the powders' production process, in the storage, and during the manufacturing of bulk parts, as investigated by D'Angelo et al. [18] and Montazeri et al. [19].

* Corresponding author at: Department of Applied Science and Technology (DISAT), Politecnico di Torino, Viale Teresa Michel 5, 15121 Alessandria, Italy.
E-mail address: marco.actis@polito.it (M. Actis Grande).

https://doi.org/10.1016/j.matdes.2024.113023
Received 19 March 2024; Received in revised form 23 April 2024; Accepted 13 May 2024
Available online 16 May 2024

Nomenclature

General

AM	Additive Manufacturing
UV–Vis-NIR	Ultraviolet–Visible-Near InfraRed
L-PBF	Laser Powder Bed Fusion
SEM	Scanning Electron Microscopy
EDS	Energy Dispersive X-ray Spectroscopy
MIM	Metal Injection Molding
UNS	Unified Numbering System
EN	European Norm

Chemometrics-related

PCA	Principal Component Analysis
PC	Principal Component
k-NN	k Nearest Neighbours
LDA	Linear Discriminant Analysis
PLS	Partial Least Squares
CV	Cross-Validation
RMSECV	Root Mean Squared Error of Cross-Validation

The highlighted problems evidence the importance of establishing a methodology to verify that powders' cross-contamination has not occurred.

Different analyses have been considered for the evaluation of cross-contamination: X-ray computed tomography (CT) and scanning electron microscopy (SEM). It is also known that X-ray photoelectron spectroscopy (XPS) and secondary ions mass spectrometry (SIMS) could be of high interest, as explained by Brandão et al. [16] and Santecchia et al. [20]. Each of the previous techniques is characterised by at least one of the following cons: complex and/or time consuming analysis, high costs, low repeatability. For this reason, another technique, UV–Vis-NIR spectroscopy, has been considered as a possible solution to this aim. As discussed by Ríos-Reina and Azcarate in their review [21], UV–Vis-NIR spectroscopy is a fast, non-invasive, low-cost technique with a simple analysis procedure, high repeatability, and it is currently already used in many fields. It is a well-known technique widely adopted to evaluate structural elucidation of organic compounds, dissociation constant of acids and bases, molecular weight determination as performed by Verma and Mishra [22], hybrid materials in catalysis, photonics, and sensing as shown by Begum et al. [23].

During the last few years, UV–Vis-NIR has already been used to evaluate metal powder absorption. Its use is fundamental for the evaluation of powders' absorbance since the parameters of production techniques like L-PBF must be set depending on the powders' laser absorptivity, as evidenced by Jiang et al. [8] and Huang et al. [24]. In case incorrect parameters are used, bulk parts will show a microstructure with un-melted powders and pores, leading to low-quality objects, as confirmed by the studies of Huang et al. [24] and Yang et al. [25].

Metal powders absorb some of the radiation when the laser hits their surface. The absorption results from 1 minus the reflectance and transmission. This last for metals is negligible since, in these wavelengths, metals have a shallow penetration depth. Therefore, absorbance is equal to 1 minus reflectance.

$$A = 1 - R \tag{1}$$

Three different absorption behaviours characterise metals, as explained by Brandau et al. [26], depending on their electronic configuration:

a) Continuous increase in absorption towards shorter wavelengths;
b) Low absorption over the entire wavelength range, apart from some inter-band transitions in the VIS-NIR range;
c) Absorption edges in the spectrum.

The first behaviour occurs mainly in transition metals such as iron or titanium. In contrast, the second is typical of metals like aluminium or magnesium, since these are polyvalent metals with filled atomic shells whereas the third one is typical for noble metals. Brandau et al. [27] and Jadhav et al. [28] discuss in depth how many factors influence metal powder absorption: the shape, the surface roughness, the presence of surface oxide, the granulometry, the size distribution and the presence of external particles.

UV–Vis-NIR spectroscopy is used as a quantitative analysis to determine the amount of solute in a solution, as performed by Lodeiro et al. [29]. The use of proper tools like chemometrics may allow to obtain deeper pieces of information for solutions and solid samples, as demonstrated by Ríos-Reina and Azcarate [21].

One of the most basic and valuable tools in multivariate analysis is the principal component analysis (PCA), which originates in the work of Pearson [30]. It evaluates the variability between samples; where the variability is high, a high amount of information is present, and the interrelations between samples and measured variables can be studied as thoroughly discussed by Oliveri et al. [31]. A new space identified by n-principal components (PCs) is generated, where the maximum variance direction represents the first principal component (PC1). All PCs are orthogonal to each other. PCA could describe, in this way, a large amount of complex information in bi-dimensional or three-dimensional plots.

Among the multivariate analysis tools, classification and regression methods could be adopted to detect the contaminant powders and the percentage of contaminant, respectively.

Oliveri et al. explain [31] that classification techniques belong to three main families:

- distance-based techniques, like *k* nearest neighbours (*k*-NN);
- probabilistic techniques, such as linear discriminant analysis (LDA);
- experience-based techniques.

k-NN is one of the most straightforward approaches for classification. The samples are considered one by one as the test object. The distances of the test object from all of the other samples in the training are evaluated, and the test object is sorted to the class with the majority representation in the k-selected samples. The parameter k represents the number of neighbours to be considered in the assignation rule, and it must be defined and optimised depending on the results obtained from the model as shown in works [32,33].

Fisher developed the linear discriminant analysis (LDA) in 1936 [34]. The means of each category and the pooled variance are computed from the training set. Class probability distributions are evaluated under two hypotheses:

1. Normal (multivariate) distribution in each class
2. The same variance–covariance for all of the classes, as highlighted by Dixon and Brereton [35].

For a quantitative prediction of cross-contamination percentage, regression techniques such as partial least squares (PLS) could be adopted; this method defines mathematical relationships between variables or groups of variables and provides models for predictions. From the values of the physical measures performed on samples, the chemical quantity in samples could be obtained using the mathematical model obtained as summarised [31]. PLS is one of the most widely adopted multivariate regression techniques since it represents a better solution to both the problems of variable number and intercorrelation. The PLS components are directions in the space of the predictors, as Wold et al. reported [36].

In this work the authors aim to demonstrate that by assessing the reflectance of powders it's possible to detect contamination even at low

Table 1
A92618 chemical composition.

Element	Al	Cu (%)	Fe (%)	Mg (%)	Ni (%)	Si (%)	Ti (%)	Zn (%)
wt% (min-max)	Balance	1.9-2.7	0.9-1.3	1.3-1.8	0.9-1.2	0.1-0.25	0.04-0.1	<0.1

Table 2
C10200 chemical composition.

Element	Cu	Fe (%)	Cr (%)	Zr (%)	Si (%)	O (%)
wt%	Balance	<0.05	–	–	–	≤0.1

amounts (<1%) qualitatively. Additionally, by creating a mathematical model using multivariate analysis, it's possible to identify the type and percentage of contaminant species. While UV–Vis-NIR spectroscopy is currently used in the powder metal field for descriptive analysis, the authors believe it could become a diagnostic tool for all metal forming techniques involving powders. In the following sections, classification and regression analyses are reported to demonstrate the predictability of UV–Vis-NIR spectroscopy. The goal is to show that this method can effectively assess the quality of powders at each stage of the forming process, ensuring reliable and consistent controls. By combining this analysis with a multivariate approach, pollutant species can also be identified. UV–Vis-NIR spectroscopy results can therefore provide detailed information on powder quality and suitability for processing, allowing operators to take corrective actions as needed throughout the process.

This work adopts the unified numbering system (UNS) alloy designation and identifies three metal powders (one for each type of metal absorption phenomenon): A92618, C10200 and S31603. A92618, an alloy based on Al-Cu system, is chosen as a representative material since it shows an absorbance behaviour closer to the elemental aluminium one compared to other Al alloys, as revealed by the analysis by Brandau et al. [26]. A92618 is generally used in applications requiring high strength and superior mechanical properties at high temperatures, where Al-Si alloys show limitations, as discussed by Schuster et al. [37]. C10200 (pure copper oxygen-free) is commonly diffused in many applications like heat transfer components and electronic applications thanks to its superior thermal and electrical conductivity, as confirmed in two studies [38,39]; moreover, its low electrochemical migration, high corrosion resistance and excellent solderability makes it of high interest as highlighted by Wu [40]. Austenitic stainless steel S31603 has an excellent corrosion-resistant property in various environments, making it an alloy used in many fields, as evidenced by Tucho et al. [41] and Sun et al. [42]. Moreover, the powders were chosen with different powder densities and granulometry. This choice was made to evaluate also systems where segregation can occur, leading to areas with a heterogeneous powders dispersion whose formation was investigated by Popplewell et al. [43] and Abouzeid and Fuerstenau [44] and how UV–Vis-NIR analysis deals with it when the laser hits these areas.

Three commercial metal powders were cross-contaminated in binary systems in different volume percentages and analysed with a UV–Vis-NIR spectroscope; their spectra were surveyed regarding their shift and shape modification compared to the uncontaminated powder ones.

Table 3
S31603 chemical composition.

Element	Fe	Cr (%)	Ni (%)	Mo (%)	C (%)	Mn (%)	Cu (%)	P (%)	S (%)	Si (%)	N (%)
wt% (min–max)	Balance	17.0–19.0	13.0–15.0	2.25–3.00	0.03	2.00	0.50	0.025	0.01	0.75	0.10

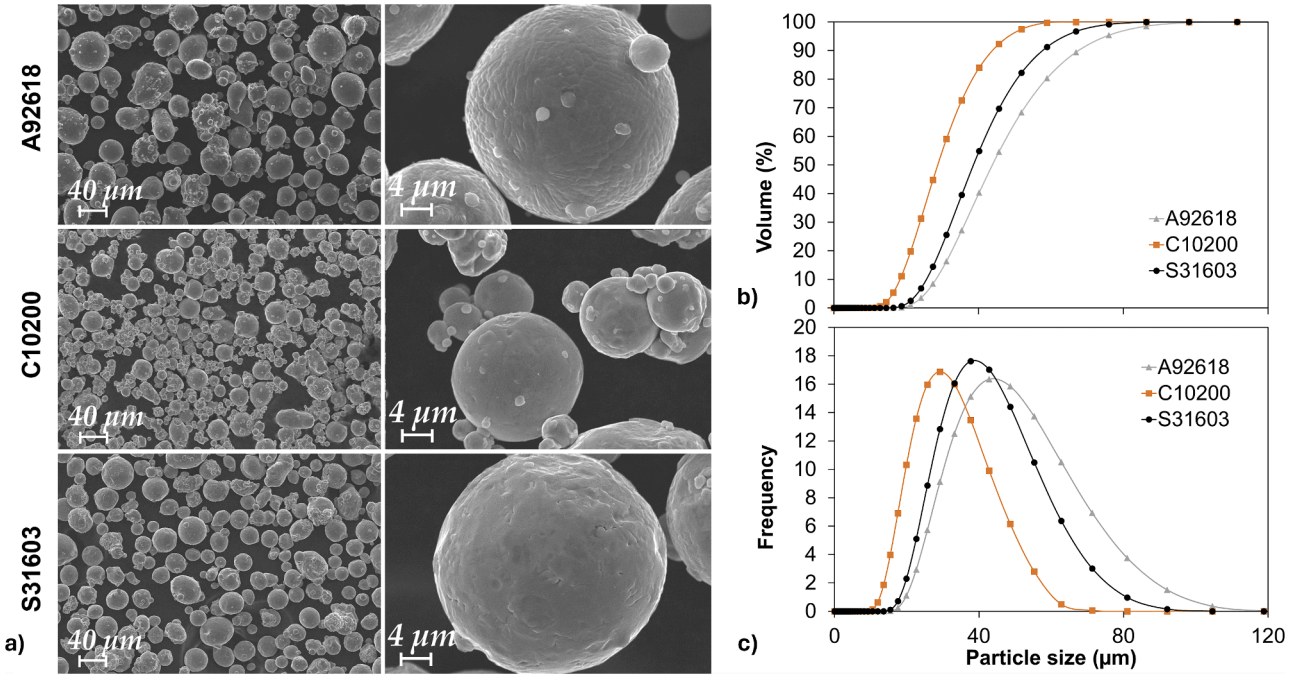

Fig. 1. A) SEM image of the surface morphology of the three different commercial powders atomised powders; b-c) size distribution of the three types of powders.

Table 4
A92618, C10200 and S31603 powder' distribution sizes.

	d_{10} (μm)	d_{50} (μm)	d_{90} (μm)
A92618	28.2	44.5	72.6
C10200	18.2	28.8	44.5
S31603	25.6	39.1	61.4

Fig. 2. Cuvettes filled with metal powders for UV–Vis-NIR analysis.

2. Materials and methods

2.1. Powder systems

A92618 (EN AW-2618) was supplied by ECKA Granules Germany GmbH, C10200 (EN Cu-OF) by Sandvik Osprey Ltd and S31603 (EN 1.4404) by EOS. The following Tables 1 to 3 show the chemical composition of the different powders, as declared by the suppliers.

The morphology of the three different powders has been analysed with SEM (Zeiss EVO 15 equipped with an Oxford Instruments Ultim Max EDS probe), Fig. 1a. Powders characterised by higher surface roughness show a higher absorbance since multiple reflections of the beam statistically occur; each time a fraction of the beam is absorbed, resulting in a lower reflectance [26]. Granulometry and particle size have been analysed through Malvern Mastersizer 3000 equipped with Aero S for dry dispersion, Fig. 1b-c. These parameters influence the absorbance of the powder; smaller particles result in higher absorbance, as demonstrated by Brandau et al. [26].

A spherical shape characterises powders, and the dimensions of their distribution sizes are reported in Table 4.

The spectrum of powders has been evaluated in the range of 250–1250 nm with UV–Vis-NIR spectrophotometer UV-2600 (Shimadzu) equipped with the Integrating Sphere Attachment ISR-2600Plus (Shimadzu).

The ISR is an integrated sphere unit with two detectors: a photomultiplier and an InGaAs detector. The measurable wavelength range is 220–400 nm in the UV range, 400–780 nm for Vis and from 780 to 1400 nm for the NIR range. The integrated sphere is coated with barium sulphate; this last in powder is also used as a reference reflectance sample. The light source change wavelength from the deuterium to the halogen lamps is set at 323 nm, and the detector change from the photomultiplier to the InGaAs detector is set at 830 nm. Two mask holders are present in the instrument, one for the target sample and one for the reference sample; they reduce the beam size in the reflectance measurement.

Cuvettes with a quartz window plate (P/N 206–89065-41 from Shimadzu) were used as powder sample holders for the analysis. The samples were prepared by mixing the metal powders in the right volume percentage, inserting them into a 2 ml Eppendorf tube and mixing for 3 min with a turbula to guarantee maximum homogeneity. Powders were then inserted in the cuvettes. Fig. 2 shows their aspects, filled with uncontaminated powders. The amount of powder inserted into the cuvette must guarantee that the light does not interact with the back of the cuvette, which would affect the measurement. Therefore, the powder thickness inside the cuvette must be at least equal to 1 mm.

The analyses were carried out using 1 scan at 0.2 nm resolution with the diffuse reflectance mode.

2.2. Cross-contamination

The three metal powders have been cross-contaminated in binary systems in different volume percentages to evaluate UV–Vis-NIR spectroscopy as an analysis for detecting cross-contamination across them. The choice of volume percentage has been made since very different specific weights characterise alloys, determining volume cross-contamination as more significant from an experimental point of view.

Five different contaminations at low concentrations and two at high concentrations were set. Low concentrations of 0.5 %, 1 %, 2 %, 4 % and 6 % have been considered, whereas 25 % and 50 % represented high concentrations of contaminants. For more streamlined sample names, alloy A92618 is identified with A, C10200 with C and S31603 with S. The samples are named as XYy, where:

X = the letter of the contaminated powder.

Y = the letter of the contaminant powder.

y = volume percentage of Y; (for brevity when the volume concentration is equal to 0.5 %, then y = 0).

For example, AC0 corresponds to a powers blend consisting of 99.5 % in volume of A92618 and 0.5 % of C10200, while CS25 is composed of 75 % in volume of C10200 and 25 % in volume of S31603. All volume concentrations are reported in Table A1 in Appendix A.

For each concentration, 3 samples were prepared; powders were measured and mixed in a turbula. Powders were then placed inside the cuvette and analysed with the UV–Vis-NIR spectrophotometer in the 250–1250 nm wavelength range to obtain reflectance spectra. The values obtained at each wavelength from the three samples were mediated and, by applying equation (1), absorbance values were then calculated.

In order to qualitatively evaluate how varying spectra with the variation of the contamination percentage, three different wavelengths were identified: 450 nm, 515 nm and 1064 nm; they correspond respectively to blue, green and red laser adopted in the laser-based AM techniques, and their absorbance values are the ones that could be found most in literature as demonstrated by the paper of Brandau et al. [26].

2.3. Chemometric analysis

Chemometric analyses were performed to evaluate the quantitative ability of the UV–Vis-NIR spectroscopy analysis in cross-contamination. Different steps have been performed to achieve this aim, and the CAT (Chemometric Agile Tool) software, developed by Leardi et al. [45], was used.

At first, all samples were analysed with the Principal Component Analysis (PCA), then classification was performed, followed by regression analysis. The classification was done to distinguish which is the contaminant species while regression was used to find out the amount of contaminant powder percentage (y); for classification and regression, samples were divided into two groups: training set and test set.

Data were treated by binning them with a bin width equal to 5 so that the data corresponding to each nm of the wavelength range considered is just 1, and it is the average between 5 values. After this, PCA was performed, followed by classification and then regression.

Specifical wavelengths were considered to perform the classification analysis to determine which would be the best for fully describing the spectra. This analysis evaluated blue, green and red laser wavelengths (450 nm, 515 nm, 1064 nm) and the first and last points of spectra (250 nm and 1250 nm). Moreover, the uncontaminated powder spectra were evaluated. The local minimal, maximal and inflexion points were detected for each one, and the wavelengths where two pure spectra intersected were considered too. Each type of powder has been taken into account separately for the test. All the samples containing the powder typology under analysis have been evaluated, except for the pure ones that can be detected with the qualitative assessment since there is no translation or modification of their spectra shape. The test set for classification is constituted of 3 samples XY at low concentration, 2 at

	Scope	Test set
Cross-contaminate systems absorbance	**Qualitative analysis** Evaluation of the spectra' modifications as a function of X and Y concentrations	All sample spectra of both uncontaminated and contaminated powders
Chemiometric: Classification k-NN and LDA	Identification of the contaminant powder Y into the mixtures XY, with X fixed	For $Y=Y_1$ and $Y=Y_2$ • 3 XYy with y≤6 • 2 XYy with y = 25 or 50 or 75 (YX25) • 3 YXy with y≤6 **Samples total** = 8 * 2 = **16**
Chemiometric: Regression - PLS	**Quantitative analysis** Evaluation of percentage contamination of mixtures XY, where X and Y are known from the classification step	• 1 X and 1 Y • 3 XYy with y≤6 • 2 XYy with y = 25 or 50 or 75 (YX25) • 3 YXy with y≤6 **Samples total = 10**

Fig. 3. Structure of the performed analysis.

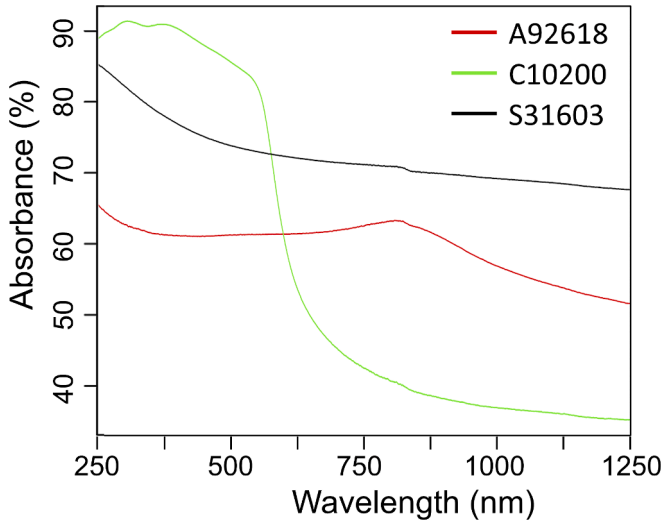

Fig. 4. UV–Vis-NIR spectra of A92618, C10200 and S31603.

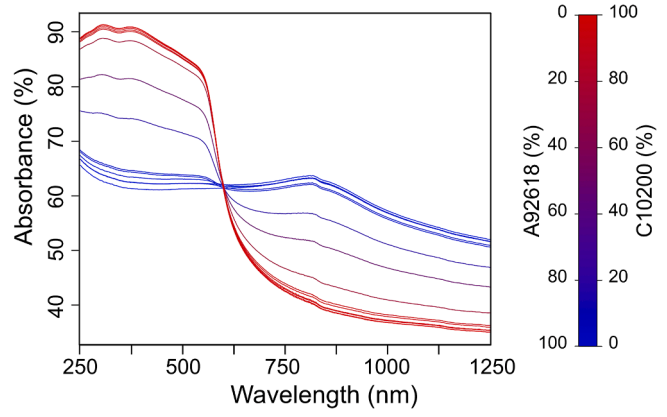

Fig. 5. Absorbance spectra of the mixed powders belonging to the A92618-C10200 system.

high concentration and for thoroughness, 3 samples at low concentration of X for a total of 8 samples. Since there are two Y, the test set is composed of 16 samples. All the other samples constitute the training material. The samples of the test set have been chosen randomly.

Two different classification methods have been evaluated: the k nearest neighbours (k-NN) and the linear discriminant analysis (LDA).

Two methods were used in LDA classification for the validation procedure: cross-validation and repeated evaluation set (100 times). The cross-validation procedure divides samples into N cancellation groups following a predetermined scheme. The model is then computed *N* times, and for each time, one of the N groups is used as the evaluation set, while the other N-1 groups are the training set. In the repeated case, also called Monte Carlo validation, a different evaluation set is created each time by random selection; this leads to a higher description of the system and a longer computational time, as discussed by Oliveri et al. [31].

After the cross-validation step, each technique performs the prediction step using the test set.

For the regression analysis, the PLS method has been adopted. PLS, repeated n times (n = 100), was used to have the best-fitting model. After performing the regression cross-validation, the global root mean squared error of cross-validation (RMSECV) was considered, and the variable elimination was repeated as long as the RMSECV decreased, as performed by Andries et al. [46]. For the regression analysis, pure samples were also taken into account. In this case, the test set is constituted of 1 sample for each pure (X and Y), 3 samples at a low concentration of X, 2 at a high concentration and 3 samples at a low concentration of Y, for a total of 10 samples. All the other samples constituted the training test. The samples of the test set have been chosen randomly. Again, firstly, the cross-validation (CV) step was performed, followed by the prediction step on the test set.

The summary of the analysis performed, their scope and their training test are reported in Fig. 3.

3. Results and discussion

3.1. Pure powders

The UV–Vis-NIR spectroscopy was performed on pure powders, and their spectra are reported in Fig. 4.

In Fig. 4, the 3 different behaviours of powders are shown:

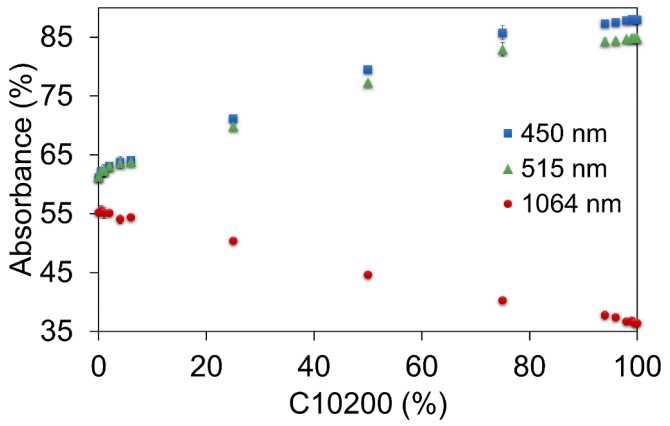

Fig. 6. Variation of absorbance at 450, 515, and 1064 nm depending on the percentage of C10200 in A92618 powders.

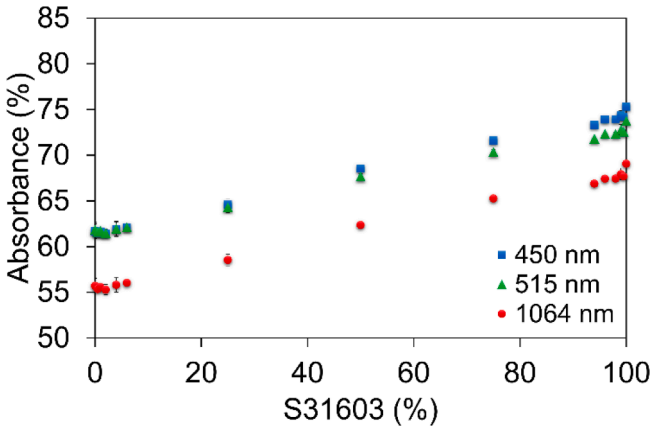

Fig. 8. Variation of absorbance at 450, 515, and 1064 nm depending on the percentage of S31603 in A92618 powders.

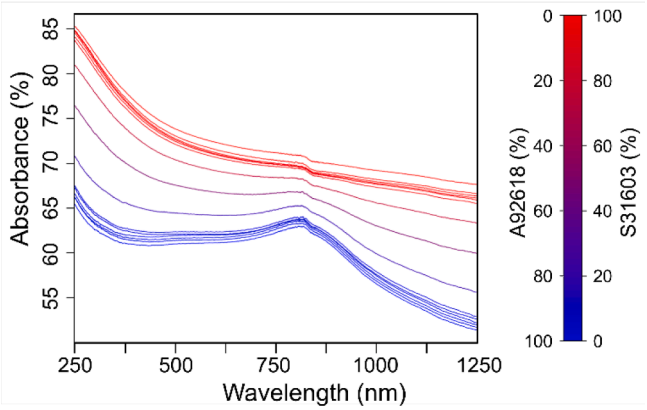

Fig. 7. Absorbance spectra of the mixed powders belonging to the A92618 – S31603 system.

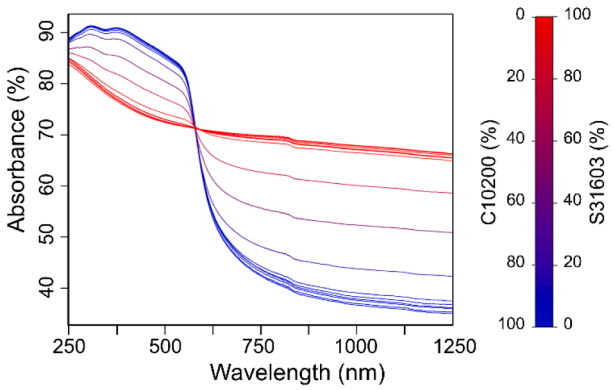

Fig. 9. Absorbance spectra of the mixed powders belonging to the C10200 – S31603 system.

- A92618 has an absorption quite constant over the entire wavelength range, apart from some inter-band transitions in the VIS-NIR range; alloying elements determine a higher absorption all over the range compared to pure aluminium;
- C10200′s spectrum has an absorption edge between 550–700 nm;
- S31603′s spectrum has a continuous increase in absorption towards shorter wavelengths.

In Fig. 4, local minimal and maximal points and the inflexion points on uncontaminated A92618, C10200 and S31603 could be detected: 270 nm, 309 nm, 345 nm, 360 nm, 378 nm, 546 nm, 652 nm, 820 nm, 942 nm, 1080 nm, and 1162 nm. The C10200 crosses both the A92618 pure spectra (around 600 nm) and S31603 one (around 580 nm); these two points were also considered for classification analysis. These were added to the 5 wavelengths detected in Section 2: 250 nm, 1250 nm, 450 nm, 515 nm, and 1064 nm, for a total of 18 data sets.

3.2. Cross-contaminate systems absorbance

3.2.1. A92618 – C10200

The system A92618 – C10200 was evaluated. Fig. 5 reports the graph with the medium spectra for each amount of contamination.

It is possible to evidence that the two pure spectra (A92618 and C10200 ones) around 600 nm have the same absorbance, and an intersection occurs between the two spectra. Moreover, all the spectra of mixed systems have the same absorbance and consequently pass from the same point of intersection. In the first part of the graph (250–599 nm), C10200 has a higher absorbance than A92618; after 600 nm, the highest absorbance is the A92618′s. The spectra of mixed powders vary depending on the percentage of pure powders constituting them: the lower the percentage of contaminating powders (B), the more similar the spectrum's trend will be to that of pure powder (A).

In Fig. 6 (values can be found in Table A2 in Appendix A), the absorbance values of the blue, green, and red laser wavelengths are reported considering the amount of C10200 contaminant in volume.

Fig. 6 shows that a linear trend characterises the relation between absorbance and relative percentages of A92618 and C10200 contained in the mixture at each wavelength analysed. Since C10200 has a higher absorbance than A92618 at low wavelengths, an increased absorbance, with the increasing of C10200 content, is determined at the blue and green wavelengths. On the contrary, for red laser wavelength, C10200 has a lower absorbance than A92618, consequentially there is a decrease of absorbance. The linear trend highlights that the spectra analysis could be qualitative and quantitative since mathematical correlation is detected in the graph.

3.2.2. A92618 – S31603

The behaviour of the system A92618- S31603 is shown in Fig. 7. S31603 shows higher absorbance than A92618 all over the UV–Vis-NIR analysed range and the pure spectra do not intersect each other.

As for the pure spectra, no intersection occurs between those of cross-contaminated powders. A shape variation of spectra can be noticed; moreover, the translation of spectra leads to no spectra intersections. In Fig. 7, looking at the y-axis at the wavelength of 250 nm, it can be noticed that the spectra of 0 %, 25 %, 50 %, 75 % and 100 % of S31603 are uniformly distributed. This indicates that a linear relationship

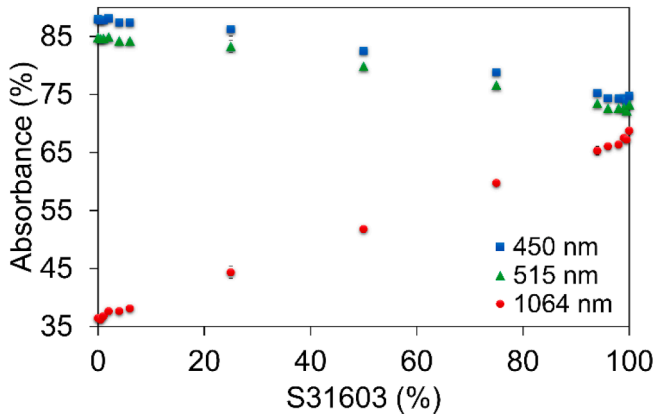

Fig. 10. Variation of absorbance at 450, 515, and 1064 nm depending on the percentage of S31603 in C10200 powders.

between absorbance and contaminant percentage is present. In order to analyse this further, the variation of absorbance has been evaluated with the increasing content of S31603 powder, as reported in Fig. 8 (Table A3 in Appendix A).

Since no intersection occurs between the spectra of uncontaminated powders and considering that S31603 has a higher absorbance all over the analysed range, the same behaviour characterises the mixtures at all 3 wavelengths. A linear trend is evidenced at all three wavelengths with a different slope, and it is increasing with the increase of S31603 powder content in the mixture.

3.2.3. C10200 – S31603

In the system C10200 – S31603, the two pure spectra intersect around 580 nm, as shown in Fig. 9.

The two pure spectra (C10200 and S31603 ones) around 580 nm have the same absorbance, determining an intersection between the two spectra. At the wavelength of 580 nm all the spectra of mixed systems are characterised by the same absorbance; at lower wavelengths, C10200 has a higher absorbance than S31603; after 580 nm, on the contrary, S31603 has a lower reflectance.

In Fig. 10 (values in Table A4 in Appendix A), it is possible to highlight that a linear trend is detected in the absorbance variation depending on the contamination percentage.

Since C10200 has a higher absorbance than S31603 at low wavelengths, a decreased absorbance, with the increase of S31603 content, is determined at the blue and green wavelengths. On the contrary, C10200 has a higher reflectance for red laser wavelength than S31603, and the absorbance increases with the increasing content of S31603.

If the graph in Fig. 10 was plotted as a function of C10200 percentage, it would result in a plot very similar to the one reported in Fig. 6: same linear trends but with a different slope.

The analysis of the three different systems (AC, AS, CS) shows that the UV–Vis-NIR technique detects the cross-contamination since a shift and a shape modification of the spectra of admixed powders occur as a function of the percentage of powders constituting the systems. Qualitative information are obtained on the percentage of contaminant powders by analysing the absorbance spectra.

Summing up, in binary systems, with an intersection point (λ_P) between pure spectra, if absorbances at two different wavelengths, one lower and one higher than λ_P, are plotted as a function of the percentage content of powder B, the trend of the two will be discord; one will increase and the other decrease. If the wavelength selected is equal to λ_P, the trend will be a line parallel to the x-axis. Instead, if no intersection occurs between pure systems, it is because one of the two powders (B) has a higher absorbance all over the range, and whatever the two wavelengths considered to compare the trend of their absorbance against the percentage content of powder B, these will show an increasing linear trend with, at most, different slopes.

In addition to what reported so far, a quantitative study on the percentage of contaminant powder can also be performed with chemometric tools. They can be used for the identification of the contaminant specie, as shown in the following sections.

3.3. Chemometric analysis – Principal Component analysis

All samples' spectra after the binning operation have been evaluated with the Principal Component Analysis. The first two components almost explain the total variance (up to 99.9 %), so only these are considered. The results are reported in Fig. 11, where the score plot reports the projection of each sample in the space defined by the new variables: the coordinate values obtained are called scores as explained by Oliveri et al. [31].

In Fig. 11 b), it is possible to notice that the different points, each representing a sample, lie on an ideal triangle: uncontaminated powders (A92618, C10200, S31603) are located on its vertices, while cross-contaminated samples (AC, AS, CS) lie on the ideal triangle's sides, in particular on the side connecting the two vertices constituted by the pure powders present in the mixture. For example, if the system taken into account is AS, A92618 and S31603 uncontaminated powders

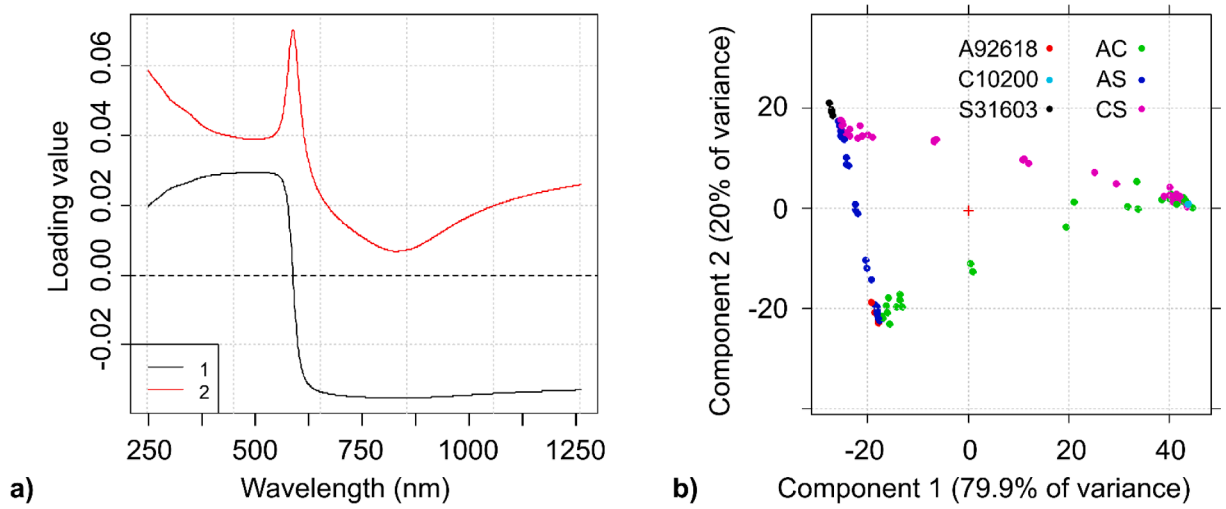

Fig. 11. PCA of all samples: a) loading plot; b) score plot.

Table 5
Percentage of correct predictions in CV for k-NN classification depending on k for samples containing A92618 powders.

	AC	AS	Total
k = 1	96.15	96.15	96.15
k = 2	92.31	92.31	92.31
k = 3	96.15	100.00	98.08
k = 4	84.62	88.46	86.54
k = 5	84.62	96.15	90.39
k = 6	80.77	92.31	86.54
k = 7	84.62	100.00	92.31

Table 6
k-NN and LDA classification results in CV and prediction for samples containing A92618 powders.

percentage Correct Predictions	k-NN			LDA		
	AC	AS	total	AC	AS	total
CV	96.2	100	98.1	96.2	100	98.1
Prediction	100	100	100	100	100	100

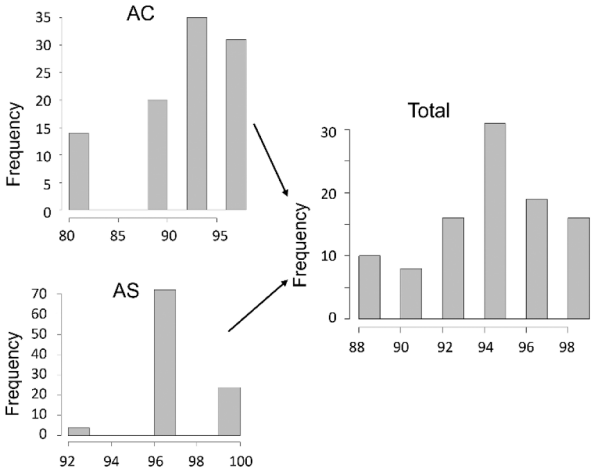

Fig. 12. Plots describing the frequency in repeated LDA classification for samples containing A92618 powders.

represent two of the three vertices, all mixtures samples AS are located on the line (side) joining A and S; the highest the content of S31603 the closer the point representing the sample will be to the S31603's vertex.

For a more comprehensive evaluation of all the systems taken into account in the following paragraphs, PCA analysis was performed on all systems; results are reported in Appendix B:

- Classification: A92618 – Fig. B1, C10200 – Fig. B2, S31603 – Fig. B3;
- Regression: A92618- C10200 system – Fig. B4, A92618-S31603 system – Fig. B5, C10200 –S31603 system – Fig. B6.

3.4. Chemometric analysis – classification

After the general PCA, classification was performed on samples to evaluate which is the contaminant powder.

3.4.1. A92618

Samples containing A92618 powders were considered for the classification analysis. The results for the different k of the k-NN analysis can be found in Table 5.

For the A92618 system, the number of neighbour samples that best fit the model to discriminate the class group for the samples belonging to

Table 7
Percentage of correct predictions for LDA classification (repeated 100 times) results in CV for samples containing A92618 powders.

	mean	min	max
AC	91.12	80.77	96.15
AS	96.92	92.31	100
Total	94.02	88.46	98.08

Table 8
Percentage of correct predictions in CV for k-NN classification depending on k for samples containing C10200 powders.

	AC	CS	total
k = 1	73.08	70.37	71.72
k = 2	65.38	59.26	62.32
k = 3	84.62	70.37	77.50
k = 4	65.38	62.96	64.17
k = 5	73.08	66.67	69.88
k = 6	65.38	59.26	62.32
k = 7	84.62	70.37	77.50

Table 9
k-NN and LDA classification results in CV and prediction for samples containing C10200 powders.

percentage Correct Predictions	k-NN			LDA		
	AC	CS	total	AC	CS	total
CV	84.6	70.4	77.5	96.2	100	98.1
Prediction	100	75.0	87.5	87.5	87.5	87.5

the A92618 system is 3, as evidenced in Table 5; k-NN classification results with k = 3 are reported in Table 6 with those of single LDA.

From the table, it can be seen that for this system, k-NN and LDA analysis provide the same results with the cross-validation step and the prediction of the test set; for this last, both models give 100 % accuracy of results. The LDA Monte Carlo validation results are reported in Fig. 12 and Table 7.

The Monte Carlo validation is highly predictive; samples contaminated with S31603 are more accurately classified than those contaminated with C10200. The highest prediction capability for the samples contaminated with S31603 could be found in the PCA plots (Fig. B1), where all the samples containing A92618 and S31603 are all aligned on a straight line, while those with C10200 are more dispersed. From the table, it is possible to highlight that using a specific set of cancellation

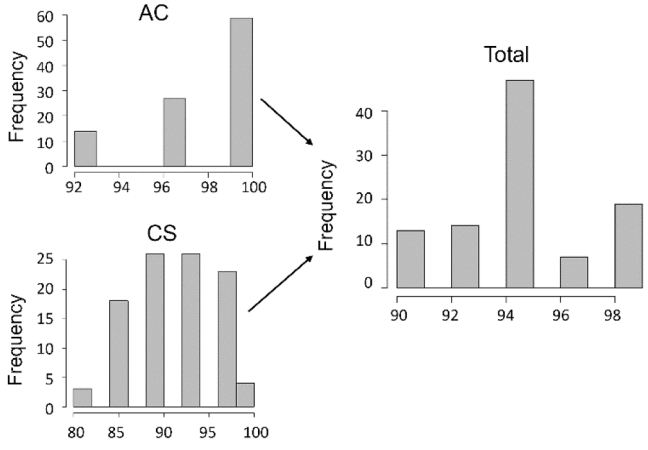

Fig. 13. Plots describing the frequency in repeated LDA classification for samples containing C10200 powders.

Table 10
Percentage of correct predictions for LDA classification (repeated 100 times) results in CV for samples containing C10200 powders.

	mean	min	max
AC	97.88	92.31	100.00
CS	91.11	81.48	100.00
Total	94.50	90.60	98.15

Table 11
Percentage of correct predictions in CV for k-NN classification depending on k for samples containing S31603 powders.

	AS	CS	Total
k = 1	96.15	92.59	94.37
k = 2	88.46	85.19	86.82
k = 3	96.15	92.59	94.37
k = 4	92.31	74.07	83.19
k = 5	96.15	81.48	88.81
k = 6	88.46	74.07	81.26
k = 7	100.00	74.07	87.03

Table 12
k-NN and LDA classification results in CV and prediction for samples containing S31603 powders.

percentage Correct Predictions	**k-NN**			**LDA**		
	AS	CS	total	AS	CS	total
CV	96.2	92.6	94.4	100	96.3	98.1
Prediction	100	87.5	93.8	100	100	100

groups with LDA results in the best performance, as indicated by the values matching the maximum ones from the Monte Carlo validation. The Monte Carlo validation involves running the Linear Discriminant Analysis (LDA) multiple times with different randomly selected sets of data. However, the best results obtained from this analysis may coincide with those of a single LDA, as seen in this specific case. Additionally, it's crucial to examine the distribution of results presented in Fig. 12. It's evident that in this scenario, the test set used by the software to conduct the single LDA corresponds to the best conditions for both AS and AC. Consequently, the overall prediction capability is also the highest.

3.4.2. C10200

Mixtures containing C10200 powders have been evaluated. The results for the different k of the k-NN analysis can be found in Table 8.

The number of neighbours that must be evaluated for samples containing C10200 powders equals 3 or 7. Both k were evaluated in the prediction model since they are equal, and k = 7 provides better prediction capability. The results of this analysis and single LDA are reported in Table 9.

For mixtures containing C10200 powders, the technique with a higher prediction ability in CV is the LDA. LDA repeated CV was performed; its results are reported in Fig. 13 and Table 10.

The set of cancellation groups used by the single LDA model provides the best result for CS samples, but it predicts AC samples less accurately compared to the mean result. This underscores the importance of the Monte Carlo validation. On average, the model performs better in identifying samples contaminated with A92618 powder. In this specific case, there are test sets where all CS samples are correctly associated, and the same applies to those belonging to AC. However, Monte Carlo validation reveals that these two occurrences don't coincide, as the total predictable capability never reaches 100 %. For instance, the set considered by the software for the single LDA shows the highest CS and total prediction ability in CV, but not for samples belonging to the AC system. This discrepancy demonstrates that achieving high predictability for one category doesn't guarantee the same for another, highlighting the complexity of the classification task.

Table 13
Percentage of correct predictions for LDA classification (repeated 100 times) results in CV for samples containing S31603 powders.

	mean	min	max
AS	94.27	88.46	100.00
CS	88.56	77.78	96.30
Total	91.41	83.12	98.15

3.4.3. S31603

The classification of mixtures with S31603 powders was performed. The results for the different k of the k-NN analysis can be found in Table 11. The best k result is k = 3; the results of this analysis and single LDA are reported in Table 12.

Once again, the LDA method resulted in a more predictive model. The results of the repeated LDA are reported in Fig. 14 and Table 13.

In this classification, the samples from the A92618-S31603 system show better classification performance, as they align more closely on a straight line in PCA plots (Fig. B 3) and are more easily associated with the mathematical model. The average accuracy of LDA classification, calculated from multiple cross-validation runs, is lower than the accuracy obtained from a single LDA analysis (as shown in Table 12). This highlights the importance of conducting repeated LDA cross-validation to ensure more reliable results. Monte Carlo validation indicates that

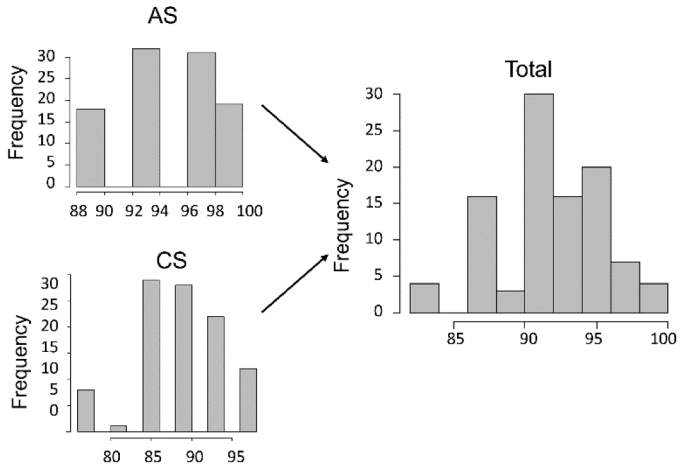

Fig. 14. Plots describing the frequency in repeated LDA classification for samples containing S31603 powders.

Table 14
Summary of percentage of correct predictions in CV and prediction for k-NN and LDA classification.

percentage Correct Predictions		A92618			C10200			S31603		
		AC	AS	total	AC	CS	total	AS	CS	Total
k-NN	CV	96.2	100	98.1	84.6	70.4	77.5	96.2	92.6	94.4
	Prediction	100	100	100	100	75.0	87.5	100	87.5	93.8
LDA	**CV– repeated (mean)**	91.1	96.9	94.0	97.9	91.1	94.5	94.3	88.6	91.4
	Prediction	100	100	100	87.5	87.5	87.5	100	100	100

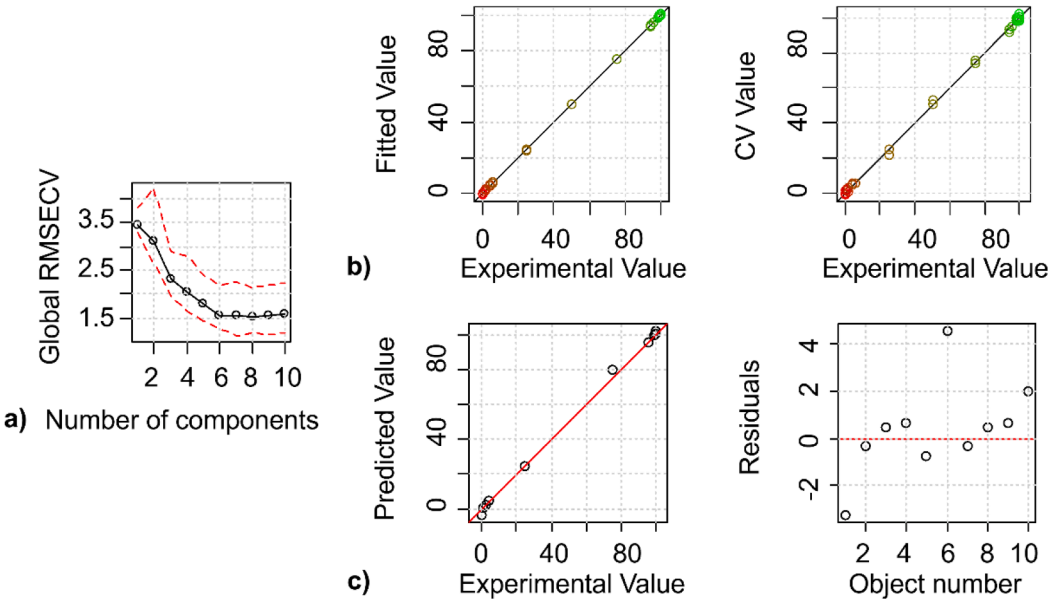

Fig. 15. A) evaluation of the global RMSECV in the regression of the AC system; b) Experimental vs calculated values of training test in the CV of the regression of system AC; c) Predicted values of test set in the regression of system AC.

Table 15
Predicted values of test set in the regression of system AC and the deviation from the expected values.

sample name	A_t	AC0_t	AC2_t	AC4_t	AC25_t	CA25_t	CA4_t	CA1_t	CA0_t	C_t
% C10200	−3.24	0.19	2.48	4.65	24.26	79.53	95.69	99.47	100.14	101.98
Deviation	−3.24	−0.31	+0.48	+0.65	−0.74	+4.53	−0.31	+0.47	+0.64	+1.98

the results obtained from the single LDA analysis belong to sets that yield the best results for cross-validation. It's essential to note that with a higher number of iterations or repetitions, the results of Monte Carlo validation could potentially vary, possibly characterized by wider distributions due to the random selection of data sets.

Table 14 presents an outline of the two different classification models applied to the various mixtures; it is possible to provide evidence that both systems offer a highly predictable ability in cross-validation and prediction.

Applying chemometrics classification techniques can provide accurate results in determining the contaminant species at a low cost.

3.5. Chemometric analysis – regression

3.5.1. A92618 – C10200

For the A92618- C10200 powder system, all the AC mixtures have been taken into account, and non-contaminated A92618 and C10200 samples have been used too. The PLS analysis has been performed considering 10 components. After the regression, the plot reported in Fig. 15a has been obtained (values can be found in Table B 1 in Appendix B): the global root mean squared error of cross-validation (RMSECV) decreases until the number of components was equal to 8. After setting the number of components equal to 8, the training set was validated. The comparison between the experimental and calculated values is reported in Fig. 15b. The two plots show no significant differences, indicating that the model calculated by the software is valid and that the analysis of spectra corresponds to their contaminant percentage. The prediction step was performed with the test set, and results are shown in Fig. 15c and Table 15.

Table 15 highlights that mixtures show predicted values very close to the real ones, with a deviation lower than ± 0.8 %, apart from the sample CA25_t. In this case, due to the different densities and granulometry characterising A92618 and C10200, powders segregation occurred, resulting in a slightly higher deviation. Considering pure powders, it can be highlighted that their deviation is locating them out of the scale, evidencing that these are negatively contaminated and consequentially, since this cannot be, they are pure. Negative percentages of contamination help their individuation among the other samples.

3.5.2. A92618 – S31603

For the A92618-S31603 powder system, non-contaminated A92618 and S31603 samples and all the AS mixtures have been taken into account. Also in this case, PLS analysis was done considering 10

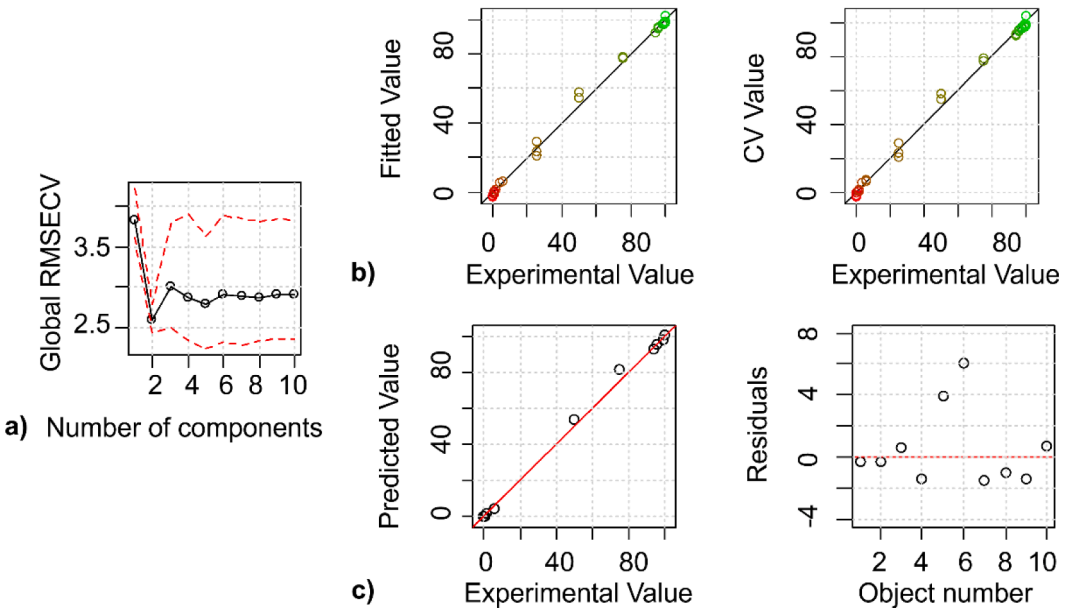

Fig. 16. A) evaluation of the global RMSECV in the regression of the AS system; b) Experimental vs calculated values of training test in the CV of the regression of system AS; c) Predicted values of test set in the regression of system AS.

Table 16
Predicted values of test set in the regression of system AS and the deviation from the expected values.

sample name	A_t	AS0_t	AS1_t	AS6_t	AS50_t	SA25_t	SA6_t	SA4_t	SA0_t	S_t
% S31603	−0.25	0.19	1.65	4.60	53.92	81.03	92.49	94.97	98.09	100.66
Deviation	−0.25	−0.31	+0.65	−1.40	+3.92	+6.03	−1.51	−1.03	−1.41	+0.66

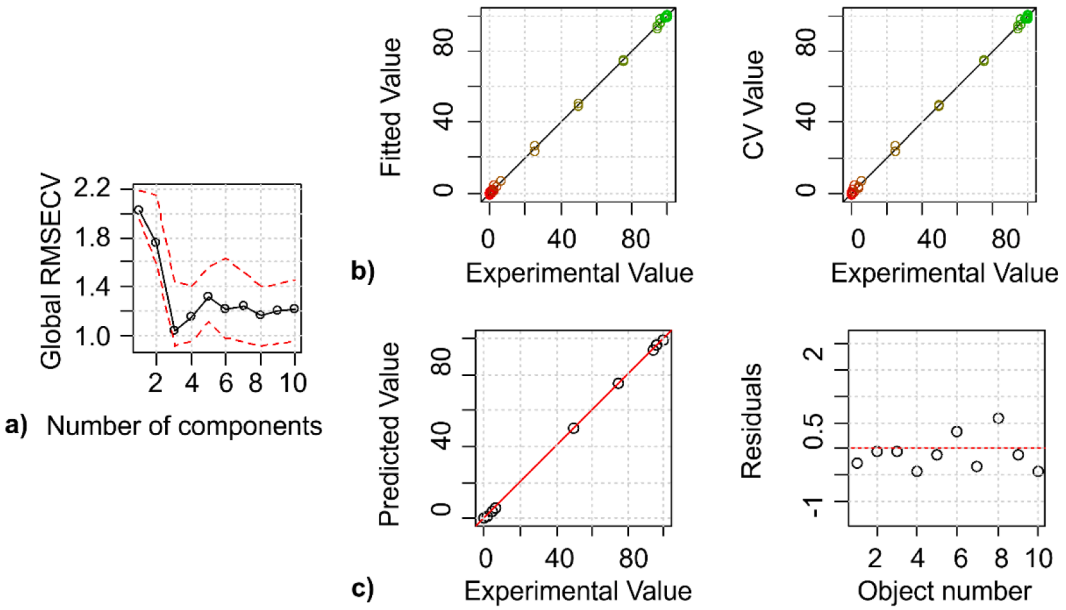

Fig. 17. A) evaluation of the global RMSECV in the regression of the CS system; b) experimental vs calculated values of training test in the CV of the regression of system CS; c) predicted values of test set in the regression of system CS.

components. Results are reported in Fig. 16a (values in Table B2 in Appendix B). From Fig. 16a, it is possible to highlight that in this system, the number of components must be set equal to 2 since this is the first local point of minimum. The validation of the training set leads to the plots shown in Fig. 16b, and the comparison of experimental and calculated values does not differ significantly. The test set was used to validate the prediction capability of the regression model. Results are shown in Fig. 16c and Table 16.

Mixtures with a low percentage of contaminant have a deviation up to ± 1.5 %. At high concentrations of cross-contamination, the prediction ability is slightly lower since it has a deviation from actual values between 4–6 %. This is correlated to the fact that A92618 granulometry

Table 17
Predicted values of test set in the regression of system CS and the deviation from the expected values.

sample name	C_t	CS1_t	CS4_t	CS6_t	CS50_t	SC25_t	SC6_t	SC4_t	SC0_t	S_t
% S31603	−0.26	0.96	3.96	5.56	49.87	75.33	93.68	96.59	99.40	99.59
Deviation	−0.26	−0.04	−0.04	−0.44	−0.13	+0.33	−0.32	+0.59	−0.10	−0.41

is similar to those of S31603, but their specific weight is very different. This can lead again to the local de-mixing of powders, originating areas with heterogeneous distribution, as previously discussed.

3.5.3. C10200 – S31603

For the C10200 −S31603 powder system, the PLS analysis has been performed considering 10 components. After the regression, the plot reported in Fig. 17a was obtained (values in Table B3 in Appendix B): the number of components has been set equal to 3. The validation of the training test evidences that no differences can be highlighted between the experimental and calculated values reported in plots, Fig. 17b. Lastly, the prediction step was performed with the test set, and the results are shown in Fig. 17c and Table 17.

The regression model in this system shows the highest predicting ability, with a deviation lower than ± 0.6 %. This system's predictable ability at high and low concentrations is comparable since a similar specific weight characterises C10200 and S31603 powders, and the powders' distribution size does not differ significantly.

Comparing the results of the three systems, it is possible to evidence that chemometrics tools applied to UV–Vis-NIR spectra result in a quantification of the percentage of cross-contamination among the different powders. Moreover, it is possible to underline that the percentage of contamination predicted is closer to the actual value as the powder's densities and granulometries of the two species constituting the system are more similar. When the density of the contaminated powder is very different from the contaminant one, especially at high percentages of cross-contamination, the occurring segregation leads to a deviation of approx. 5 % instead of 0.5–1.5 %, depending on the systems.

Chemometric analysis can detect, with a precision higher than 85 %, the contaminant specie among those considered potential in the different process steps. Once the contaminant powder has been identified, it is possible to determine its amount with the regression analysis.

4. Conclusions

UV–Vis-NIR spectroscopy is evaluated as a fast, non-invasive, and low-cost technique for detecting cross-contamination in metal powders. The spectrum shape changes with increasing contamination percentage, showing shifts and modifications. The spectra of contaminated powders become more similar to pure powders as the content of the contaminating powder increases. Specific wavelengths show a linear trend between contaminant percentage and absorbance variation. This method allows qualitative analysis of cross-contamination and can be used in Powder Metallurgy to assess process conditions and maintain control. For known contaminants, a multivariate approach can be used, employing classification models like LDA and k-NN, which show over 85 % prediction capability. Regression analysis is applied to identify contaminant type and concentration. PLS analysis is effective for qualitative analysis, especially when powders have similar densities. Chemometric tools combined with UV–Vis-NIR spectroscopy allow for contaminant identification and quantitative analysis, aiding in the recovery of cross-contaminated powders based on user knowledge.

CRediT authorship contribution statement

Marta Ceroni: Writing – review & editing, Writing – original draft, Visualization, Methodology, Investigation, Formal analysis, Data curation, Conceptualization. **Federico Simone Gobber:** Writing – review & editing, Validation, Supervision, Methodology, Investigation, Conceptualization. **Marco Actis Grande:** Writing – review & editing, Supervision, Resources, Methodology, Funding acquisition, Conceptualization.

Declaration of competing interest

The authors declare that they have no known competing financial interests or personal relationships that could have appeared to influence the work reported in this paper.

Data availability

Data will be made available on request.

Acknowledgements

Financial support was given from the Italian Government - Ministry of University and Research - within the Ministerial Decree n° 1062/2021 which received funding from the FSE REACT-EU – PON Ricerca e Innovazione 2014–2020.

Appendix A:. Systems evaluation and their absorbance

Table A1
Samples names and their powder concentrations.

	Volume % A92618	Volume % C10200		Volume % A92618	Volume % S31603		Volume % C10200	Volume % S31603
AC0	99.5	0.5	AS0	99.5	0.5	CS0	99.5	0.5
AC1	99.0	1.0	AS1	99.0	1.0	CS1	99.0	1.0
AC2	98.0	2.0	AS2	98.0	2.0	CS2	98.0	2.0
AC4	96.0	4.0	AS4	96.0	4.0	CS4	96.0	4.0
AC6	94.0	6.0	AS6	94.0	6.0	CS6	94.0	6.0
AC25	75.0	25.0	AS25	75.0	25.0	CS25	75.0	25.0
AC50	50.0	50.0	AS50	50.0	50.0	CS50	50.0	50.0
CA25	25.0	75.0	SA25	25.0	75.0	SC25	25.0	75.0
CA6	6.0	94.0	SA6	6.0	94.0	SC6	6.0	94.0
CA4	4.0	96.0	SA4	4.0	96.0	SC4	4.0	96.0

(*continued on next page*)

Table A1 (*continued*)

	Volume % A92618	Volume % C10200		Volume % A92618	Volume % S31603		Volume % C10200	Volume % S31603
CA2	2.0	98.0	SA2	2.0	98.0	SC2	2.0	98.0
CA1	1.0	99.0	SA1	1.0	99.0	SC1	1.0	99.0
CA0	0.5	99.5	SA0	0.5	99.5	SC0	0.5	99.5

Table A2
Absorbance of the different concentrations of contamination between A92618 and C10200 powders for the selected laser wavelength.

% C10200	450 nm			515 nm			1064 nm		
0	61.13	±	0.03	61.31	±	0.00	55.21	±	0.07
0.5	62.21	±	0.70	62.33	±	0.73	55.58	±	0.77
1	62.22	±	1.07	62.31	±	1.07	55.14	±	0.97
2	63.08	±	0.71	63.06	±	0.67	55.14	±	0.29
4	63.80	±	0.91	63.58	±	0.88	54.08	±	0.79
6	64.06	±	0.20	63.83	±	0.22	54.40	±	0.37
25	71.11	±	0.40	69.88	±	0.35	50.40	±	0.32
50	79.51	±	0.21	77.33	±	0.14	44.64	±	0.28
75	85.73	±	1.21	82.94	±	1.14	40.27	±	0.55
94	87.29	±	0.50	84.32	±	0.44	37.75	±	0.73
96	87.49	±	0.39	84.46	±	0.29	37.42	±	0.35
98	87.78	±	0.05	84.73	±	0.07	36.70	±	0.29
99	88.03	±	0.19	84.93	±	0.28	36.81	±	0.65
99.5	88.00	±	0.14	84.90	±	0.21	36.41	±	0.62
100	87.94	±	0.03	84.81	±	0.03	36.41	±	0.23

Table A3
Absorbance of the different concentrations of contamination between A92618 and S31603 powders for the selected laser wavelength.

% S31603	450 nm			515 nm			1064 nm		
0	61.67	±	0.80	61.88	±	0.82	55.70	±	0.83
0.5	61.43	±	0.18	61.61	±	0.18	55.35	±	0.19
1	61.65	±	0.12	61.78	±	0.12	55.57	±	0.14
2	61.37	±	0.53	61.51	±	0.56	55.29	±	0.56
4	61.90	±	0.80	61.98	±	0.80	55.81	±	0.79
6	62.10	±	0.23	62.13	±	0.25	56.04	±	0.21
25	64.59	±	0.62	64.32	±	0.59	58.53	±	0.66
50	68.51	±	0.31	67.69	±	0.28	62.37	±	0.30
75	71.59	±	0.29	70.35	±	0.26	65.26	±	0.29
94	73.32	±	0.14	71.81	±	0.15	66.89	±	0.16
96	73.91	±	0.27	72.37	±	0.29	67.42	±	0.24
98	73.92	±	0.16	72.34	±	0.15	67.44	±	0.13
99	74.34	±	0.54	72.77	±	0.57	67.93	±	0.64
99.5	74.18	±	0.15	72.59	±	0.15	67.69	±	0.12
100	75.30	±	0.29	73.76	±	0.29	69.06	±	0.26

Table A4
Absorbance of the different concentrations of contamination between C10200 and S31603 powders for the selected laser wavelength.

% S31603	450 nm			515 nm			1064 nm		
0	87.94	±	0.12	84.89	±	0.16	36.45	±	0.30
0.5	87.79	±	0.10	84.65	±	0.17	36.22	±	0.30
1	87.81	±	0.24	84.71	±	0.24	36.80	±	0.55
2	88.15	±	0.22	84.90	±	0.35	37.65	±	0.56
4	87.40	±	0.23	84.26	±	0.32	37.65	±	0.35
6	87.40	±	0.27	84.28	±	0.20	38.15	±	0.42
25	86.23	±	1.13	83.31	±	1.07	44.36	±	1.02
50	82.52	±	0.11	79.88	±	0.06	51.80	±	0.32
75	78.84	±	0.13	76.63	±	0.12	59.74	±	0.06
94	75.26	±	0.20	73.48	±	0.26	65.32	±	0.74
96	74.35	±	0.19	72.67	±	0.14	66.06	±	0.59
98	74.34	±	0.50	72.65	±	0.45	66.36	±	0.57
99	74.39	±	0.33	72.80	±	0.34	67.52	±	0.29
99.5	73.86	±	0.25	72.25	±	0.26	67.20	±	0.34
100	74.78	±	0.15	73.30	±	0.14	68.76	±	0.14

Appendix B:. Chemometric

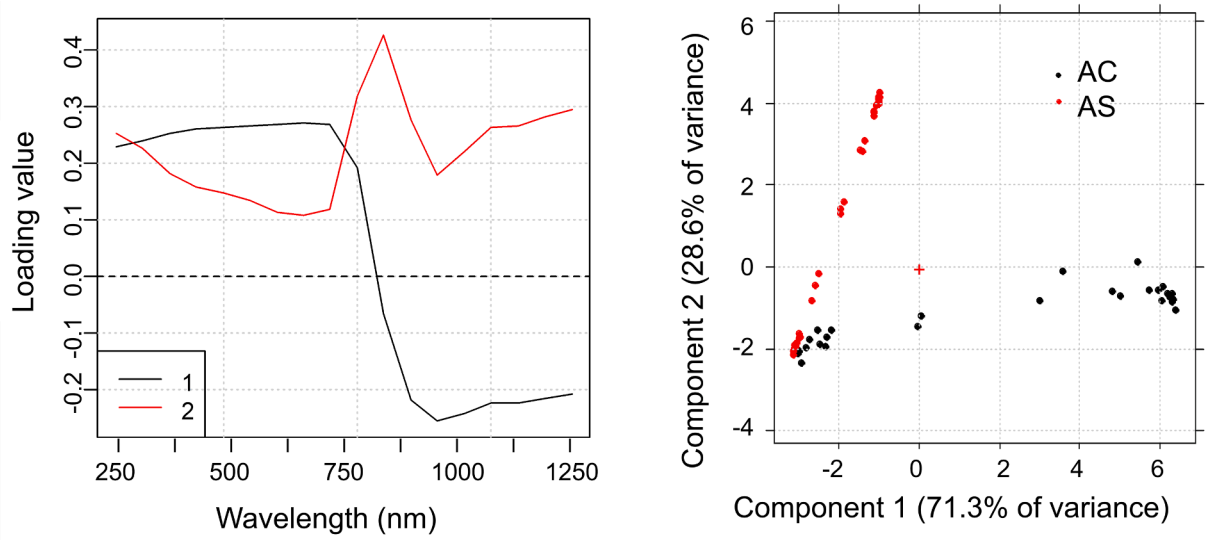

Fig. B1. PCA of mixtures containing A92618 powders: sx) loading plot; dx) score plot

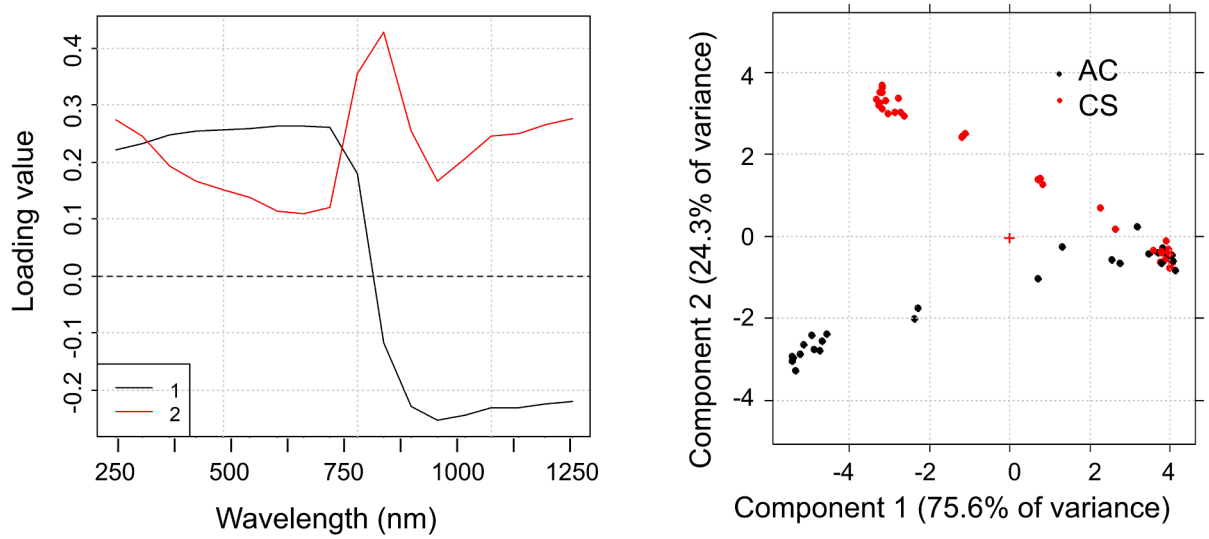

Fig. B2. PCA of mixtures containing C10200 powders: sx) loading plot; dx) score plot

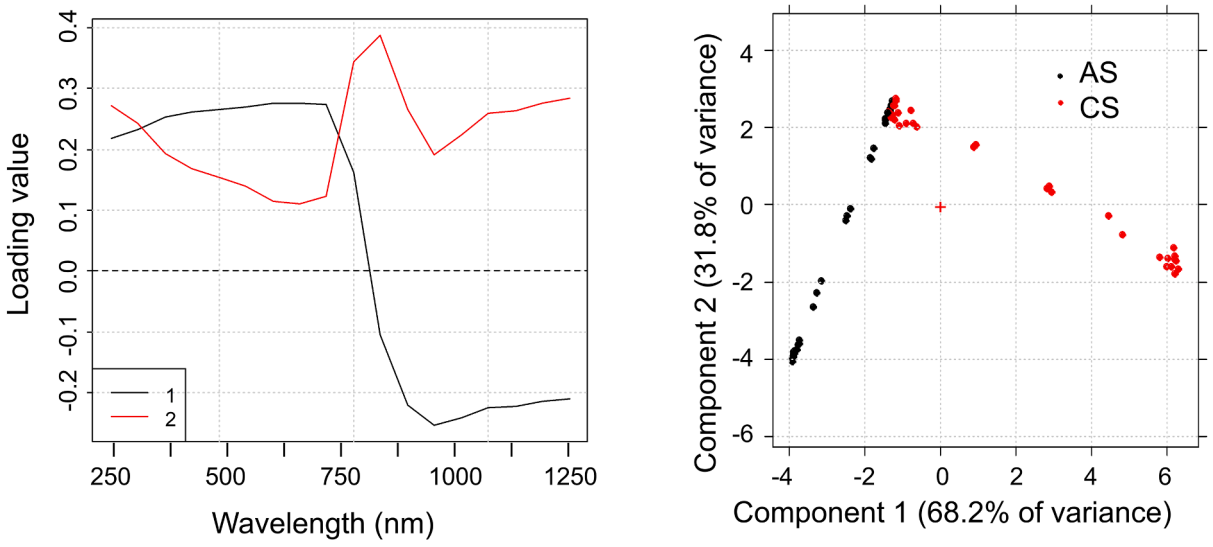

Fig. B3. PCA of mixtures containing S31603 powders: sx) loading plot; dx) score plot

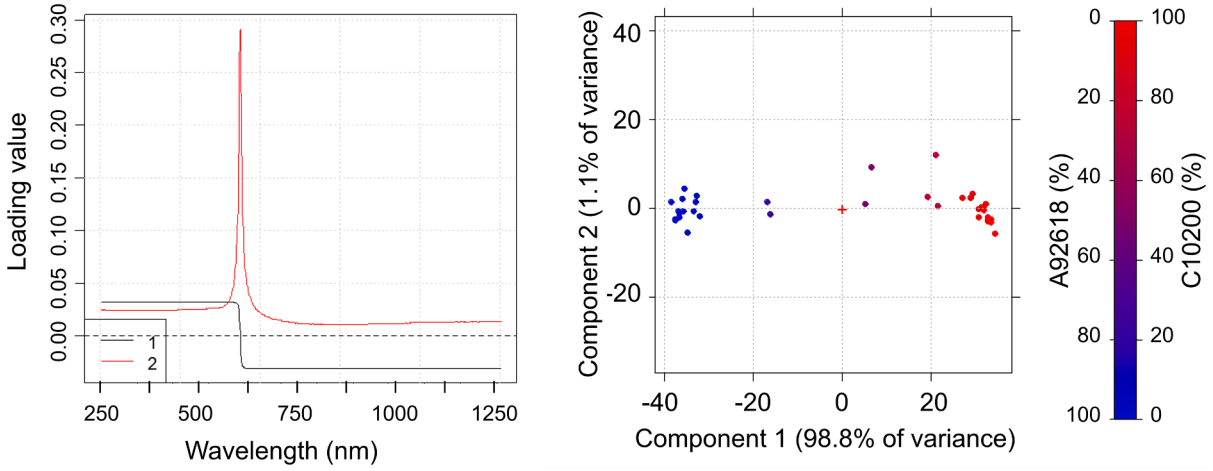

Fig. B4. PCA of samples containing A92618 and C10200 powders: sx) loading plot; dx) score plot

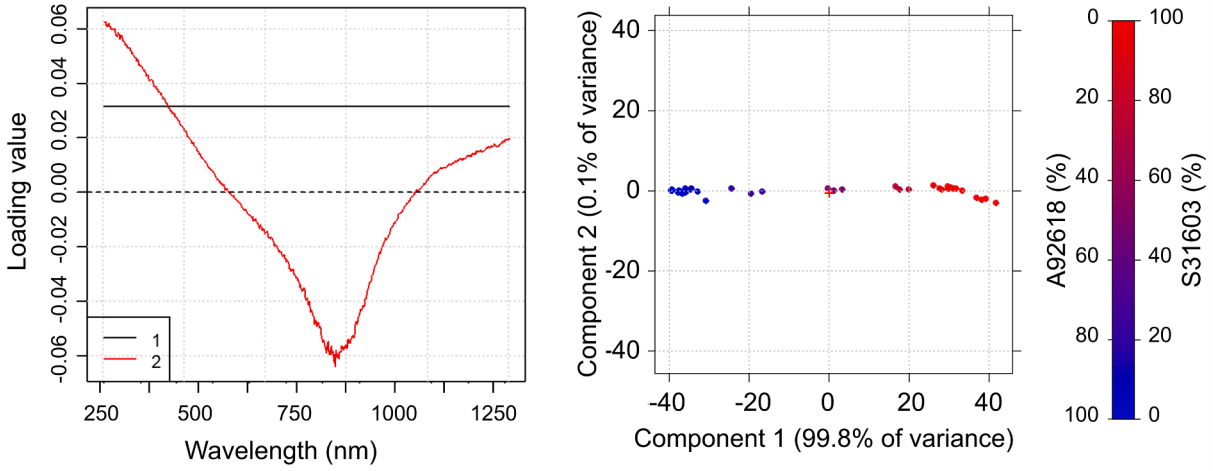

Fig. B5. PCA of samples containing A92618 and S31603 powders: sx) loading plot; dx) score plot

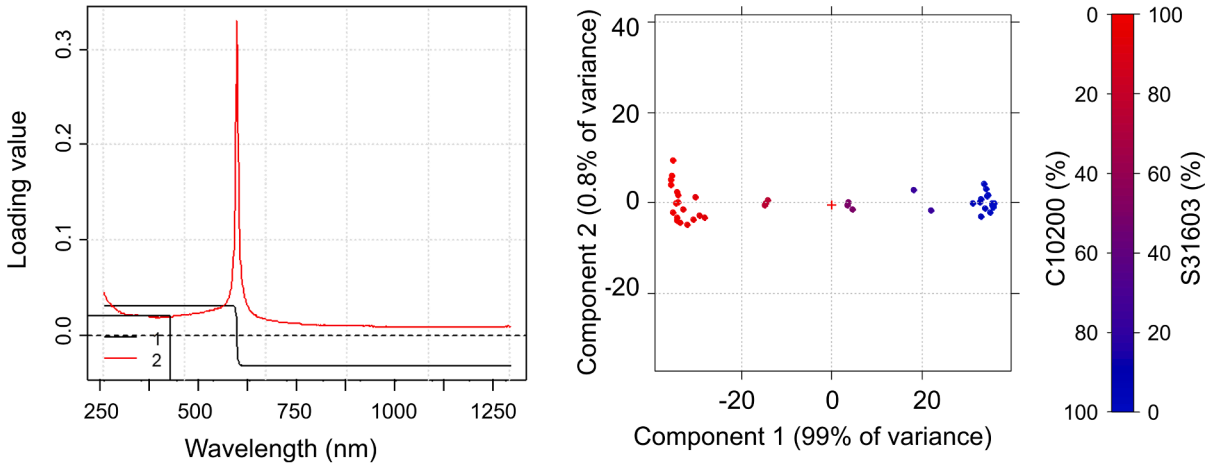

Fig. B6. PCA of samples containing C10200 and S31603 powders: sx) loading plot; dx) score plot

Table B1
Results of PLS analysis on the AC system.

components	1	2	3	4	5	6	7	8	9	10
CV% Explained Variance	99.38	99.5	99.72	99.79	99.83	99.87	99.87	99.88	99.88	99.87
Global RMSECV	3.45	3.11	2.31	2.03	1.79	1.57	1.56	1.52	1.55	1.58

Table B2
Results of PLS analysis on the AS system.

components	1	2	3	4	5	6	7	8	9	10
CV% Explained Variance	99.23	99.64	99.52	99.56	99.58	99.55	99.55	99.56	99.55	99.55
Global RMSECV	3.81	2.59	3.01	2.87	2.79	2.91	2.89	2.87	2.90	2.90

Table B3
Results of PLS analysis on the CS system.

components	1	2	3	4	5	6	7	8	9	10
CV% Explained Variance	99.79	99.84	99.95	99.93	99.91	99.93	99.92	99.93	99.93	99.93
Global RMSECV	2.02	1.76	1.03	1.14	1.31	1.21	1.24	1.16	1.19	1.20

References

[1] S.V. Zavadiuk, P.I. Loboda, T.O. Soloviova, I.I. Trosnikova, O.P. Karasevska, Optimisation of the Sintering Parameters for Materials Manufactured by Powder Injection Molding, Powder Metall. Met. Ceram. 59 (1–2) (2020) 22–28, https://doi.org/10.1007/s11106-020-00134-9.

[2] S.Z. Soong, W.L. Lai, A.N. Kay Lup, Atomisation of metal and alloy powders: Processes, parameters, and properties, AIChE J. 69 (11) (2023) 1–13, https://doi.org/10.1002/aic.18217.

[3] M. Dzemko, B. Engelmann, J. Hartmann, J. Schmitt, Toward shifted production strategies through additive manufacturing: A technology and market review for changing value chains, Procedia CIRP 86 (March) (2020) 228–233, https://doi.org/10.1016/j.procir.2020.01.029.

[4] A. Basir, A.B. Sulong, N.H. Jamadon, N. Muhamad, U.B. Emeka, Process Parameters Used in Macro/Micro Powder Injection Molding: An Overview, Met. Mater. Int. 27 (7) (2021) 2023–2045, https://doi.org/10.1007/s12540-020-00767-w.

[5] S.R. Narasimharaju, et al., A comprehensive review on laser powder bed fusion of steels: Processing, microstructure, defects and control methods, mechanical properties, current challenges and future trends, J. Manuf. Process. 75 (January) (2022) 375–414, https://doi.org/10.1016/j.jmapro.2021.12.033.

[6] W. Abd-Elaziem, et al., On the current research progress of metallic materials fabricated by laser powder bed fusion process: a review, J. Mater. Res. Technol. 20 (2022) 681–707, https://doi.org/10.1016/j.jmrt.2022.07.085.

[7] S. Chowdhury, et al., Laser powder bed fusion: a state-of-the-art review of the technology, materials, properties & defects, and numerical modelling, J. Mater. Res. Technol. 20 (2022) 2109–2172, https://doi.org/10.1016/j.jmrt.2022.07.121.

[8] Q. Jiang *et al.*, "A review on additive manufacturing of pure copper," *Coatings*, vol. 11, no. 6, 2021, doi: 10.3390/coatings11060740.

[9] K. Asano, et al., Laser metal deposition of pure copper on stainless steel with blue and IR diode lasers, Opt. Laser Technol. 107 (2018) 291–296, https://doi.org/10.1016/j.optlastec.2018.06.012.

[10] H. Siva Prasad, F. Brueckner, J. Volpp, A.F.H. Kaplan, Laser metal deposition of copper on diverse metals using green laser sources, Int. J. Adv. Manuf. Technol. 107 (3–4) (2020) 1559–1568, https://doi.org/10.1007/s00170-020-05117-z.

[11] X. Wang, et al., Functional metal powders: Design, properties, applications, and prospects, Mater. Sci. Eng. B 280 (June) (2022) 115708, https://doi.org/10.1016/j.mseb.2022.115708.

[12] C. Monti, M. Turani, K. Papis, M. Bambach, A new Al-Cu alloy for LPBF developed via ultrasonic atomisation, Mater. Des. 229 (2023) 111907, https://doi.org/10.1016/j.matdes.2023.111907.

[13] H. Shi, et al., In-situ spherical TiB2/Cu composite powder: A new method of liquid phase reaction coupled with gas atomisation, Mater. Charact. vol. 191, no. July (2022) 112096, https://doi.org/10.1016/j.matchar.2022.112096.
[14] F.C. da Silva, M.L. de Lima, G.F. Colombo, Evaluation of a Mathematical Model Based on Lubanska Equation to Predict Particle Size for Close-Coupled Gas Atomization of 316L Stainless Steel, Mater. Res. 25 (2022), https://doi.org/10.1590/1980-5373-mr-2021-0364.
[15] G. Sarriegui, J.M. Martín, N. Burgos, M. Ipatov, A.P. Zhukov, J. Gonzalez, Effect of neodymium content and niobium addition on grain growth of Nd-Fe-B powders produced by gas atomisation, Mater. Charact. 172 (December) (2021) 110844, https://doi.org/10.1016/j.matchar.2020.110844.
[16] A. D. Brandão *et al.*, "Challenges in Additive Manufacturing of space parts: Powder feedstock cross-contamination and its impact on end products," *Materials (Basel).*, vol. 10, no. 5, 2017, doi: 10.3390/ma10050522.
[17] B. Zhang, Y. Li, Q. Bai, Defect Formation Mechanisms in Selective Laser Melting: A Review, Chinese J. Mech. Eng. (english Ed. 30 (3) (2017) 515–527, https://doi.org/10.1007/s10033-017-0121-5.
[18] G. D'Angelo, E. Resebo, D. B. Pedersen, and O. Harrysson, "Challenges and quality implications of feedstock cross-contamination of metal powders: An industrial perspective," *Proc. - 2018 ASPE euspen Summer Top. Meet. Adv. Precis. Addit. Manuf.*, pp. 277–280, 2018.
[19] M. Montazeri, R. Yavari, P. Rao, and P. Boulware, "In-process monitoring of material cross-contamination defects in laser powder bed fusion," *J. Manuf. Sci. Eng. Trans. ASME*, vol. 140, no. 11, 2018, doi: 10.1115/1.4040543.
[20] E. Santecchia, P. Mengucci, A. Gatto, E. Bassoli, S. Defanti, G. Barucca, Cross-Contamination Quantification in Powders for Additive Manufacturing: A Study on Ti-6Al-4V and Maraging Steel, Materials (basel) 12 (15) (Jul. 2019) 2342, https://doi.org/10.3390/ma12152342.
[21] R. Ríos-Reina and S. M. Azcarate, "How Chemometrics Revives the UV-Vis Spectroscopy Applications as an Analytical Sensor for Spectralprint (Nontargeted) Analysis," *Chemosensors*, vol. 11, no. 1, 2023, doi: 10.3390/chemosensors11010008.
[22] G. Verma, M. Mishra, Development and Optimisation Of UV-Vis Spectroscopy - A Review, World J. Pharm. Res. 7 (11) (2018) 1170–1180, https://doi.org/10.20959/wjpr201811-12333.
[23] R. Begum, et al., Applications of UV/Vis Spectroscopy in Characterization and Catalytic Activity of Noble Metal Nanoparticles Fabricated in Responsive Polymer Microgels: A Review, Crit. Rev. Anal. Chem. 48 (6) (Nov. 2018) 503–516, https://doi.org/10.1080/10408347.2018.1451299.
[24] J. Huang, et al., Pure copper components fabricated by cold spray (CS) and selective laser melting (SLM) technology, Surf. Coatings Technol. vol. 395, no. May (2020) 125936, https://doi.org/10.1016/j.surfcoat.2020.125936.
[25] K.V. Yang, P. Rometsch, C.H.J. Davies, A. Huang, X. Wu, Effect of heat treatment on the microstructure and anisotropy in mechanical properties of A357 alloy produced by selective laser melting, Mater. Des. 154 (2018) 275–290, https://doi.org/10.1016/j.matdes.2018.05.026.
[26] B. Brandau, A. Da Silva, C. Wilsnack, F. Brueckner, and A. F. H. Kaplan, "Absorbance study of powder conditions for laser additive manufacturing," *Mater. Des.*, vol. 216, no. March, 2022, doi: 10.1016/j.matdes.2022.110591.
[27] B. Brandau, F. Brueckner, A.F.H. Kaplan, Absorbance determination of a powder bed by high resolution coaxial multispectral imaging in laser powder bed fusion, Opt. Laser Technol. 168 (June) (2023) 2024, https://doi.org/10.1016/j.optlastec.2023.109780.
[28] S.D. Jadhav, J. Vleugels, J. Kruth, J. Van Humbeeck, K. Vanmeensel, Mechanical and electrical properties of selective laser-melted parts produced from surface-oxidised copper powder, Mater. Des. Process. Commun. 2 (2) (Apr. 2020) 1–11, https://doi.org/10.1002/mdp2.94.
[29] P. Lodeiro, E.P. Achterberg, M.S. El-Shahawi, Detection of silver nanoparticles in seawater at ppb levels using UV–visible spectrophotometry with long path cells, Talanta 164 (November) (2017) 257–260, https://doi.org/10.1016/j.talanta.2016.11.055.
[30] K. Pearson, "LIII. On lines and planes of closest fit to systems of points in space," *London, Edinburgh, Dublin Philos. Mag. J. Sci.*, vol. 2, no. 11, pp. 559–572, Nov. 1901, doi: 10.1080/14786440109462720.
[31] P. Oliveri, C. Malegori, and M. Casale, *Chemometrics: multivariate analysis of chemical data*. 2020.
[32] N.S. Altman, An Introduction to Kernel and Nearest-Neighbor Nonparametric Regression, Am. Stat. 46 (3) (Aug. 1992) 175–185, https://doi.org/10.1080/00031305.1992.10475879.
[33] T. Cover, P. Hart, Nearest neighbor pattern classification, IEEE Trans. Inf. Theory 13 (1) (Jan. 1967) 21–27, https://doi.org/10.1109/TIT.1967.1053964.
[34] R.A. Fisher, The use of multiple measurements in taxonomic problems, Ann. Eugen. 7 (2) (Sep. 1936) 179–188, https://doi.org/10.1111/j.1469-1809.1936.tb02137.x.
[35] S.J. Dixon, R.G. Brereton, Comparison of performance of five common classifiers represented as boundary methods: Euclidean Distance to Centroids, Linear Discriminant Analysis, Quadratic Discriminant Analysis, Learning Vector Quantization and Support Vector Machines, as dependent on, Chemom. Intell. Lab. Syst. 95 (1) (2009) 1–17, https://doi.org/10.1016/j.chemolab.2008.07.010.
[36] S. Wold, M. Sjöström, L. Eriksson, PLS-regression: A basic tool of chemometrics, Chemom. Intell. Lab. Syst. 58 (2) (2001) 109–130, https://doi.org/10.1016/S0169-7439(01)00155-1.
[37] M. Schuster, A. De Luca, R. Widmer, X. Maeder, C. Leinenbach, Processability, microstructure and precipitation of a Zr-modified 2618 aluminium alloy fabricated by laser powder bed fusion, J. Alloys Compd. 913 (2022) 165346, https://doi.org/10.1016/j.jallcom.2022.165346.
[38] T.Q. Tran, et al., 3D printing of highly pure copper, Metals (basel) 9 (7) (2019) 12–20, https://doi.org/10.3390/met9070756.
[39] L. Constantin, Z. Wu, N. Li, L. Fan, J.F. Silvain, Y.F. Lu, Laser 3D printing of complex copper structures, Addit. Manuf. vol. 35, no. March (2020) 101268, https://doi.org/10.1016/j.addma.2020.101268.
[40] S. Wu, Preparation of ultra-fine copper powder and its lead-free conductive thick film, Mater. Lett. 61 (16) (2007) 3526–3530, https://doi.org/10.1016/j.matlet.2006.11.128.
[41] W.M. Tucho, V.H. Lysne, H. Austbø, A. Sjolyst-Kverneland, V. Hansen, Investigation of effects of process parameters on microstructure and hardness of SLM manufactured SS316L, J. Alloys Compd. 740 (2018) 910–925, https://doi.org/10.1016/j.jallcom.2018.01.098.
[42] Z. Sun, X. Tan, S.B. Tor, C.K. Chua, Simultaneously enhanced strength and ductility for 3D-printed stainless steel 316L by selective laser melting, NPG Asia Mater. 10 (4) (2018) 127–136, https://doi.org/10.1038/s41427-018-0018-5.
[43] L.M. Popplewell, O.H. Campanella, V. Sapru, M. Peleg, Theoretical comparison of two segregation indices for binary powder mixtures, Powder Technol. 58 (1) (1989) 55–61, https://doi.org/10.1016/0032-5910(89)80007-5.
[44] A.Z.M. Abouzeid, D.W. Fuerstenau, Mixing-demixing of particulate solids in rotating drums, Int. J. Miner. Process. 95 (1–4) (2010) 40–46, https://doi.org/10.1016/j.minpro.2010.03.006.
[45] G. Leardi, R.; Melzi, C.; Polotti, "CAT (Chemometric Agile Tool)." p. freely downloadable from, [Online]. Available: http://gruppochemiometria.it/index.php/software.
[46] J.P.M. Andries, Y. Vander Heyden, L.M.C. Buydens, Improved variable reduction in partial least squares modelling by Global-Minimum Error Uninformative-Variable Elimination, Anal. Chim. Acta 982 (2017) (2017) 37–47, https://doi.org/10.1016/j.aca.2017.06.001.